Supercurrent interference in HgTe-wire Josephson junctions

Wolfgang Himmler [1,*,†] Ralf Fischer [1,*] Michael Barth [2] Jacob Fuchs [2] Dmitriy A. Kozlov [1,3]
Nikolay N. Mikhailov,[3] Sergey A. Dvoretsky [3] Christoph Strunk,[1] Cosimo Gorini [4] Klaus Richter [2] and Dieter Weiss [1,†]

[1]*Institute of Experimental and Applied Physics, University of Regensburg, D-93040 Regensburg, Germany*
[2]*Institute of Theoretical Physics, University of Regensburg, D-93040 Regensburg, Germany*
[3]*A. V. Rzhanov Institute of Semiconductor Physics, Novosibirsk 630090, Russia*
[4]*Université Paris-Saclay, CEA, CNRS, SPEC, 91191 Gif-sur-Yvette, France*

Wires made of topological insulators (TI) are a promising platform for searching for Majorana bound states. These states can be probed by analyzing the fractional ac Josephson effect in Josephson junctions with the TI wire as a weak link. An axial magnetic field can be used to tune the system from trivial to topologically nontrivial. Here, we investigate the oscillations of the supercurrent in such wire Josephson junctions as a function of the axial magnetic field strength and different contact transparencies. Although the current flows on average parallel to the magnetic field we observe $h/2e$, $h/4e$, and even $h/8e$ periodic oscillations of the supercurrent in samples with lower contact transparencies. Corresponding tight-binding transport simulations using a Bogoliubov–de Gennes model Hamiltonian yield the supercurrent through the Josephson junctions, showing in particular the peculiar $h/4e$-periodic oscillations observed in experiments. A further semiclassical analysis based on Andreev-reflected trajectories connecting the two superconductors allows us to identify the physical origin of these oscillations. They can be related to flux-enclosing paths winding around the TI nanowire, thereby highlighting the three-dimensional character of the junction geometry compared to common planar junctions.

I. INTRODUCTION

$U_0 = 600 \, \text{meV nm}$ In wires made from a three-dimensional topological insulator (3DTI) the topological surface states form a two-dimensional conducting electron layer that envelops the bulk. The energy spectrum of these wires features a gap at zero magnetic field which closes when an axial magnetic flux of $\phi_0 = h/2e$ threads the wire cross section [1–5]. With closing of the gap, a nondegenerate perfectly transmitting mode appears, rendering the wire's band structure topologically nontrivial. Whereas semiconductor wires with strong spin-orbit interaction are the prevailing material platform so far to search for Majorana bound states ([6–9] and references therein), mesoscopic wires made of TI material are a promising alternative [10–16]. Recent experiments utilizing the fractional Josephson effect in HgTe-based Josephson junctions (JJ) indeed provided evidence that the 4π-periodic supercurrents observed for an axial magnetic flux $> \phi_0/4$ are of topological origin [17]. In these experiments two superconducting contacts are placed across a HgTe wire with the TI wire constituting the normal region forming a JJ.

So far, semiconductor wires with strong spin-orbit interaction have been the prevailing system class to search for topological superconductivity. The JJ built from such wire structures and their behavior in a magnetic field have been investigated, for instance, in Refs. [18–24]. Related work is also available on JJs made from Cd_3As_2 [25] or Bi_2Se_3 [26] wires and $(Bi, Sb)_2Te_3$ nanoribbons [27].

Here, we investigate the evolution of supercurrent interference in HgTe wire-based JJs as a function of an axial magnetic field. The supercurrent flows between the two superconducting contacts along the TI and is driven by the difference φ of the superconducting phase between the two contacts. In the presence of an axial magnetic field the supercurrent amplitude oscillates as a result of interference between Andreev bound states acquiring different phases along their quasiclassical trajectory between the superconducting contacts [28]. In the case of a junction with the magnetic field perpendicular to the supercurrent, the supercurrent oscillations are described by $I_c(\phi) = I_c(0)|\sin(\pi\phi/\phi_0)/(\pi\phi/\phi_0)|$, identical to the Fraunhofer pattern of a single slit experiment. Such a pattern is not expected for the TI-wire JJ mentioned above, since the current flows on average parallel to the magnetic field and the shortest ballistic trajectories should not pick up any phase from the magnetic flux. Remarkably, we find oscillations in the supercurrent which are $h/2e$, $h/4e$, and even $h/8e$ periodic, thus constituting a highly unusual interference pattern. While $h/2e$ oscillations have been observed in the supercurrent of diffusive Aharonov-Bohm rings in a perpendicular magnetic field [29], the interference mechanism is different here because the average current flows parallel to the magnetic field direction, and transport is mostly ballistic. Below we
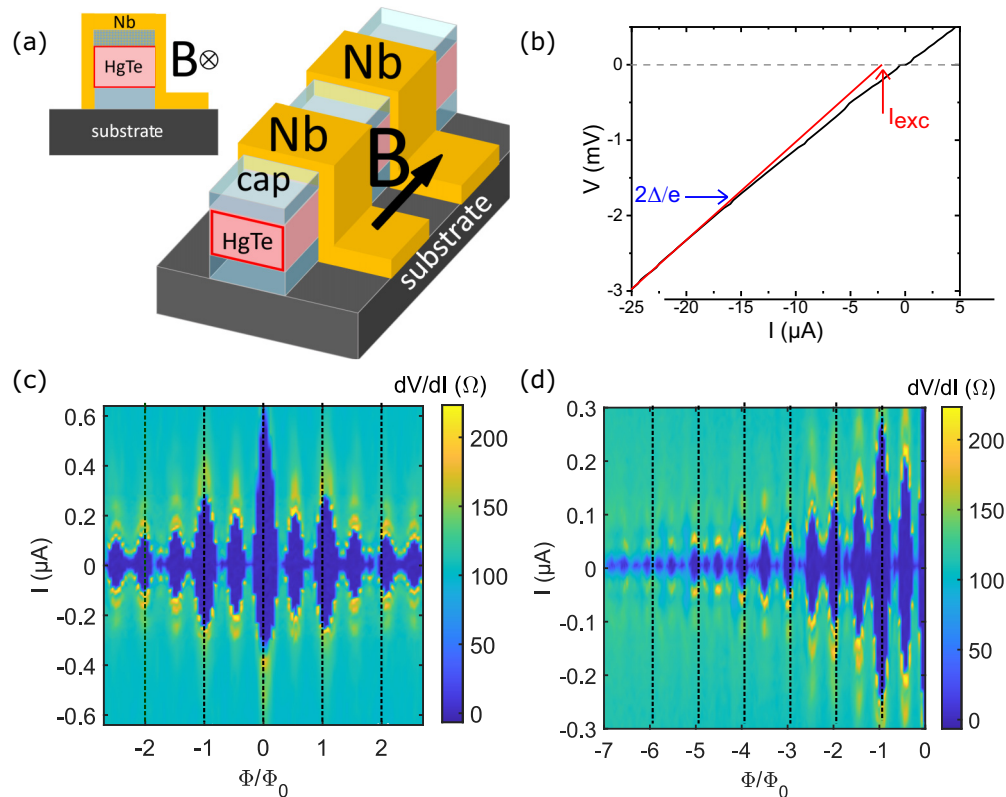

FIG. 1. Sample layout, excess current, and critical current vs. magnetic field B. (a) Cartoon of the sample layout showing the HgTe wire and the two Nb contacts which form the Josephson junction in axial cut and top view. The niobium leads are in direct contact with the top and side surface of the HgTe. The topological surface states are shown in red. The magnetic field is oriented parallel to the axis of the wires. (b) I-V trace of nanowire G (black trace) for $B = 0$ at a temperature of 27 mK. For high bias voltages, the slope represents the normal-state resistance R_N, while for lower voltages Andreev reflections influence the trace resulting in an excess current $I_{exc} = 2.2\,\mu$A. The superconducting gap Δ can be extracted from the curve as the trace starts to deviate from the constant normal-state resistance (red curve) if $eV < 2\Delta \approx 1.8$ mV. With these values the parameter $Z \approx 0.98$ is estimated. Thus, the transparency is given by $D \approx 0.51$. (c) Color map of the differential resistance dV/dI of sample G as a function of the current I and the magnetic flux ϕ/ϕ_0 ($\phi_0 = h/2e$). For sample G, ϕ/ϕ_0 corresponds to $B \approx 36$ mT. Superconducting regions are shown in blue. The critical current oscillates with a period $\phi_0/2$, while the side maxima at $\phi = \phi_0$ are most pronounced. (d) Color map of the differential resistance dV/dI of sample G up to higher values of the magnetic flux. For $\phi/\phi_0 > 3$, additional maxima appear resulting in a $\phi_0/4$ periodicity.

relate these findings, both experimentally and theoretically in a consistent way, to the three-dimensional JJ geometry and the coupling of the superconducting contacts to the TI wire.

II. DEVICE PARAMETERS AND EXPERIMENTAL SETUP

We considered nine devices (labeled A–J, ordered by descending JJ transparency D) made from wafers with an 80 nm thick, strained HgTe film, which is grown on CdTe by molecular beam epitaxy. A thin $Cd_{0.7}Hg_{0.3}Te$ buffer layer was introduced in between to improve the quality of the samples [30]. Finally, the wafers are capped by $Cd_{0.7}Hg_{0.3}Te$ and CdTe. Figure 1(a) a sketches the wafer structure and the device. Typically, the Fermi level μ is located at the top of the valence band, and surface electrons as well as bulk holes coexist. The electron density is of order $n_e \sim 10^{11}$ cm^{-2}. Additionally, In-doping was added to the $Cd_{0.7}Hg_{0.3}Te$ layers for specific wafers (samples D, G). This increases the electron density up to one order of magnitude, since the Fermi level μ is shifted to the conduction band. While bulk electrons and holes may contribute to the supercurrent (see [17] and

corresponding Supplemental Material) they play no role in the effect discussed here, as interference of bulk states does not cause, e.g., $h/2e$-periodic oscillations. We fabricate the nanowires using electron beam lithography and wet-chemical etching [17,31]. Due to the wet-chemical etching, the wires have a trapezoidal cross section. In the following, we use the average width, which typically ranges between 500 nm to 700 nm. The wire perimeter is always shorter than the phase coherence length, which is of the order of several microns [31], and transport is thus coherent. The superconducting Nb ($\sim$60 nm–80 nm) contacts are placed on the surface of HgTe after removing the capping layers by wet-chemical etching. To enhance contact quality, we clean the HgTe surface by gentle *in situ* Ar$^+$-sputtering and add a thin Ti layer ($\sim$3 nm), grown *in situ* by thermal evaporation, below the Nb. As Nb tends to oxidize, we add a thin layer of Pt ($\sim$3 nm) to protect the Nb. The distance between adjacent superconducting contacts is between 50 nm to 240 nm. The samples are cooled down in a dilution refrigerator with a base temperature of 27 mK. The B-field is aligned parallel to the wire's axis so that the magnetic flux through the wire is $\phi = BA$, where A is the

TABLE I. Sample transparencies and geometries. Junction width w, length L, and width W_S of the deposited superconducting niobium fingers for samples A–J, ordered by sample transparency D.

Sample	A	B	C	D	E	F	G	H	J
D	0.70	0.66	0.64	0.63	0.62	0.57	0.51	0.49	0.43
w [nm]	450	900	570	600	470	700	700	540	520
L [nm]	50	160	100	180	65	70	110	40	240
W_S [μm]	1.3	1.3	1.3	1.3	2.3	4.3	0.6	4.3	0.6

cross-sectional area of the wire. The measurements are taken using standard dc techniques, while the dc lines are filtered by π-filters at room temperature and Ag-epoxy filters [32] as well as RC-filters in the mixing chamber. The differential resistance dV/dI is measured by superimposing the dc bias with a small ac signal using lock-in amplifiers.

The transparency of the superconducting contacts is determined by voltage-biased measurements. An I-V trace, exemplary shown for sample G, is plotted in Fig. 1(b). The slope of the trace stays constant and represents the normal-state resistance R_n for bias voltages $V > 1.8$ mV, while for lower voltages Andreev reflections modify the slope [33,34]. The change of the resistance gives an estimation for the superconducting gap of Nb $\Delta = eV/2 \approx 0.95$ meV. The additional current flowing across the junction is the excess current $I_{exc} = 2.2$ μA. With the extracted values we calculate $eI_{exc}R_n/\Delta$, and extract the dimensionless parameter Z which describes the average transparency $D = 1/(1 + Z^2)$ using the expression of Niebler et al. [35], which is based on the work of Flensberg et al. [36] and the OBTK theory [34]. The typical measurement error to determine D is about 2%. Inserting the values of sample G, we get $Z \approx 0.98$ and $D \approx 0.51$.[1] An overview of the individual sample geometries and transparencies is displayed in Table I.

III. EXPERIMENTAL RESULTS

In a Josephson junction, a magnetic field parallel to the current direction is expected to act as a pair-breaker [37–39]. In this scenario, the critical current of the device decreases monotonously with increasing magnetic field strength. For some of our devices, however, we found a strong modulation of the critical current I_C as a function of the axial magnetic field B. Figure 1(c) presents a color map of the differential resistance dV/dI for sample G as a function of current I and magnetic flux ϕ, threading the cross-sectional area of the nanowire. This device has a critical current $I_C \approx 600$ nA and shows the most prominent oscillations of I_C. With the width of the wire $w \approx 700$ nm, one superconducting flux quantum $\phi_0 = h/2e$ corresponds to $B \approx 36$ mT. Blue regions in the color map illustrate superconducting states. The pattern displays maxima of I_C for $\phi = n \cdot \phi_0/2$ with n an integer, while I_C is fully suppressed in between them. Furthermore,

---

[1] We are aware that OBTK theory fails for low junction transparencies, because it does not correctly take into account interferences from multiple reflections (see, e.g., [13–15] in the supplement to [17]).

the maxima at multiples of ϕ_0 are more pronounced than the $\phi_0/2$ maxima. Data of the same device up to higher fluxes are shown in Fig. 1(d). Here, additional maxima at $\phi = n \cdot \phi_0/4$, $n \in \mathbb{Z}$, appear. The $h/4e$ periodicity eventually changes to $h/8e$ at higher magnetic fields. The envelope of this pattern can be ascribed to the expected pair-breaking mechanism. We note at this point that roughly $h/2e$ periodic oscillations were observed by Stampfer et al. and ascribed to oscillations of the transmission due to the conventional Aharonov-Bohm effect [24]. Nonmonotonic behavior of $I_C(B)$ with multiple nodes and lobes but without clear periodicity were observed in semiconductor nanowire JJs in an axial field [19,20].

Only a fraction of the investigated junctions show an oscillatory interference pattern of the critical current as a function of the flux, while the critical current monotonously decreases with the magnetic field for other samples. Even the exact shape and periodicity of the pattern, if it exists, differs for various devices. Therefore, we will analyze the emergence of the $I_C(B)$ oscillations in the following for different experimental parameters like contact transparency and gate voltage.

A. Gated devices

Figure 2(c) shows the data of sample J. This device has a critical current $I_C = 136$ nA and an average transparency $D = 0.43$, while one flux quantum $\phi_0 = h/2e$ corresponds to $B \approx 50$ mT. For this sample we also observe $I_C(\phi)$ oscillations. However, only maxima at $\phi = n \cdot \phi_0$ are visible leading to a $h/2e$ periodicity. For more detailed studies, a top gate was added to the junction. This allows to investigate the $I_C(\phi)$ oscillations as function of the gate voltage V_G. The structure of a gated device is sketched in Fig. 2(a). An insulator made of $\sim$30 nm SiO_2, grown by plasma enhanced chemical vapor deposition, and $\sim$100 nm Al_2O_3, grown by atomic layer deposition, was deposited above the junction. The top-gate voltage V_G is applied via a metallic Ti/Au layer. Figure 2(b) shows the critical current I_C as a function of the top-gate voltage V_G. By tuning V_G from 0 V to 3 V, I_C increases by a factor $\sim$1.7. Figure 2(d) illustrates $dV/dI(\phi, I)$ of sample J for $V_G = 3$ V. Additional maxima appear at $\phi = (2n + 1) \cdot \phi_0/2$ in contrast to the data at $V_g = 0$. Hence, the $h/4e$ periodicity is recovered by increasing V_G. This observation emphasizes that the $h/2e$ oscillations are the dominating ones and are observable for any V_G. The maxima at $\phi = (2n + 1) \cdot \phi_0/2$ cannot be resolved for $V_g = 0$ due to the low I_C at these positions. By increasing V_G, the number of contributing channels increases and the increased I_C enables to resolve I_C at $\phi = (2n + 1) \cdot \phi_0/2$. Compared to sample G, however, $I_C(\phi)$ oscillations with a period $h/8e$ are not observable, although the transparency of the devices are similar. Sample G was fabricated from a doped wafer. Its electron density, and thus the number of transport channels contributing to the signal, is much higher than in the undoped sample J, even when the latter is gated at high voltages. This suggests that for observing higher harmonics in the $I_C(\phi)$ oscillations a sufficiently large number of transport channels is necessary.

B. Influence of the transparency

In addition to differences in geometry, the transparency of the superconductor/nanowire interface is the decisive
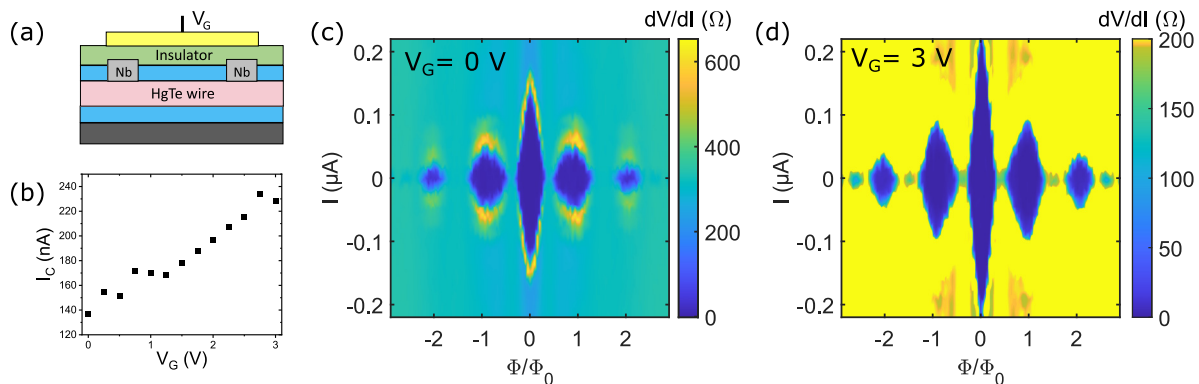
FIG. 2. Gate dependence of $I_C(B)$ oscillations. (a) Sketch of the sample layout. An insulator and a metallic top gate is placed on top of the junction. (b) The critical current I_C increases for higher gate voltages V_G. (c) Color map of the differential resistance dV/dI of sample J as a function of the current I and the magnetic flux ϕ/ϕ_0 at $V_G = 0$. The critical current oscillates with a period of ϕ_0. (d) The corresponding color maps at $V_G = 3$ V. Additional oscillations of I_C appear recovering the $\phi_0/2$ periodicity.

parameter that differentiates the devices studied. Figure 3 shows color maps of the differential resistance dV/dI as a function of the normalized current I/I_C for several samples with different transparency. The transparency was calculated using the I-V characteristics, as explained above and explicitly demonstrated for sample G. Here, it should be mentioned that the extracted transparency gives a value averaged over all contributing transport channels. Thus, it can vary locally at the superconductor/nanowire interface. In Fig. 3, the color maps are ordered by the device transparency, descending from higher to lower values from top left to bottom right, (a) → (i). Moreover, the labeling of the devices A–J follows the labeling in panels (a)–(i). Thus, devices A and B have the highest transparencies, $D \approx 0.70$ and $D \approx 0.66$, among the samples investigated. For these high-transparency devices the critical current I_C monotonously decays with increasing magnetic flux ϕ. For samples with slightly lower transparency $D \approx 0.64$ and $D \approx 0.63$, as in samples C and D, the monotonic decrease of the critical current still prevails but an additional shoulder comes out. This shoulder can be considered as a precursor of the supercurrent interference appearing at still lower transparencies. The oscillations start for device E ($D \approx 0.62$). Initially, I_C decreases and is almost fully suppressed below $\phi = \phi_0$. Then, I_C increases again and shows a maximum around $\phi = \phi_0$. The oscillations become more pronounced for samples F ($D \approx 0.57$), G ($D \approx 0.51$), H ($D \approx 0.49$), and J ($D \approx 0.43$) which have an even lower transparency.

These samples show clear $I_C(B)$ oscillations with periodicities $h/2e$ or $h/4e$. For samples G and J, the maxima appear exactly at positions $\phi = n \cdot \phi_0/2$ and $\phi = n \cdot \phi_0$, respectively, while the positions are slightly shifted for devices E and F, where the observed oscillation periods deviate by about 10 percent of a flux quantum from $h/4e$ and $h/2e$. For sample H, the observed periodicity is approximately 20 percent smaller than what one would expect from geometry. These deviations occur in samples with much wider superconducting contacts (see Table I), suggesting that the larger contacts might affect the flux distribution in the junction.

Based on these experimental observations we conclude that the transparency D is a phenomenological indicator that determines whether $I_C(B)$ oscillations occur or not. The oscillations appear preferentially for samples with low average

transparency, while they are fully absent for high transparencies.

IV. THEORY

To proceed we summarize the desiderata and key aspects of the physical problem from a more theory-oriented point of view:

(i) there must be sufficiently many open surface channels between the two superconducting electrodes to ensure a fairly high I_C;

(ii) a number of open channels must be sensitive to the flux threading the nanowire cross section, otherwise no ϕ-periodicity would show up;

(iii) imperfect contacts, representing barriers for the transport electrons, suppress contributions from flux-insensitive channels relative to flux-sensitive ones.

Based on these premises we first define the model geometry, sketched in Fig. 4 and introduced in detail below. An assumption that will turn out to be critical is that the Nb fingers induce superconductivity only close to the contact regions (shaded green areas in Fig. 4), i.e., the nanowire bottom surface remains normal conducting.[2] We will later demonstrate that modes formed by Andreev retro-reflection (partially) winding around the circumference of the 3DTI nanowire pick up an Aharonov-Bohm phase and lead to the experimentally observed supercurrent oscillations. To reach our conclusions we combine semiclassical analytics with tight-binding numerical simulations. Semiclassics allow us to identify the fundamentals of the transport problems in terms of families of electronic paths which enclose (or do not enclose) a magnetic flux. This picture is validated by rigorous quantum transport simulations based on a tight-binding implementation of the corresponding Bogoliubov–de Gennes (BdG) Hamiltonian, see below. Our analysis shows that the relevant aspects of the problem are geometrical (nonplanar surface conduction, winding vs. straight propagation, nanowire perimeter not fully

_____

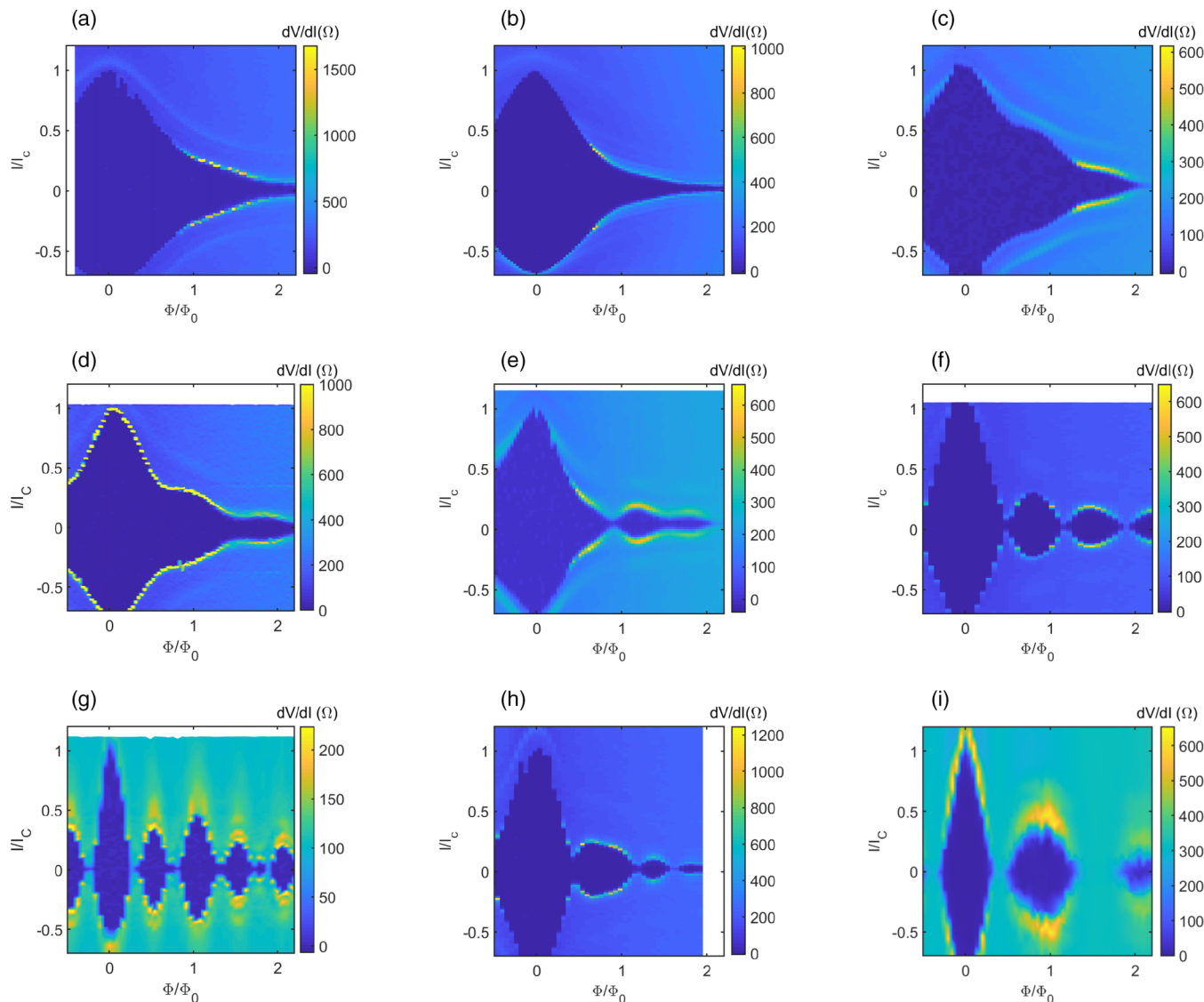[2]Except for the highest-quality samples, see the discussion in Sec. V.

FIG. 3. Impact of sample transparency on $I_C(B)$ oscillations. Color maps of the differential resistance dV/dI as a function of the current normalized I/I_c and the magnetic flux ϕ/ϕ_0 for different samples. The color maps are ordered by decreasing transparency of the junctions, with the highest transparency shown in (a) to the lowest in (i). (a), (b) Samples A and B with high transparency ($D \approx 0.70$ and $D \approx 0.66$) show no oscillations as a function of the magnetic field. (c), (d), (e) Intermediate transparencies in samples C, D, E ($D \approx 0.64$, $D \approx 0.63$, and $D \approx 0.62$, respectively): the shape of the critical current contour starts to deviate and first nodes and antinodes are observable. (f), (g), (h), (i) Samples F–J with the lowest transparencies ($D \approx 0.57$ to $D \approx 0.43$) show distinct oscillations as a function of applied magnetic field.

superconducting), while the Dirac or trivial (quadratic) nature of the carriers seems to play a secondary role.

A. Geometry and model

The upper panel of Fig. 4 shows the model geometry of the 3D nanowire JJ and the lower panel its unrolled surface. In the figure, w and h denote the nanowire width and height, L the junction length, and W_S the width of the superconducting contacts. We also introduce the perimeter $P = 2w + 2h$ and the interfacial boundary $C = w + 2h$ which describes the length of the perimeter covered by the superconducting contacts.

For the samples used in the experiment the detailed structure of the interfaces between normal and superconducting parts is not known; presumably they are rather inhomogeneous with locally varying transparencies. Since we do not

have access to the transparencies at microscopic scales, we minimize the number of phenomenological parameters by using a simple effective model with δ-like barriers at the interfaces between normal and superconducting parts,

$$U(z, s) = U_0 \Theta(s) \Theta(w + 2h - s)[\delta(z) + \delta(z - L)], \quad (1)$$

in the transverse direction only. These barriers are marked in orange in Fig. 4. They account for the fact that the supercurrent oscillations appear in the less transparent junctions; see Fig. 3. Indeed, the barriers turn out to be essential for the observation and understanding of the supercurrent oscillations with a flux-periodicity of $h/4e$. Note that the presence of barriers which are stronger on the upper nanowire section and weaker at the bottom are compatible with the fabrication process, in particular with the
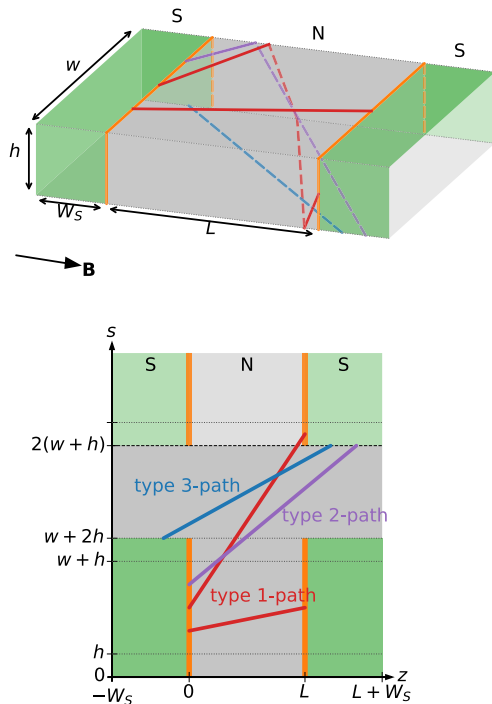
FIG. 4. Geometry of the system used in the theoretical model. The upper panel shows a 3D sketch of the nanowire Josephson junction while the lower panel is a 2D sketch of the rolled out and periodically continued nanowire surface. Regions with induced superconductivity are shaded green, normal conducting regions gray. Superconductivity is not induced around the whole circumference, the bottom area is still considered as normal conducting. Additional barriers used in the model are marked as vertical orange lines in the lower panel. The different type of retro-reflected paths arising from our semiclassical analysis, Sec. IV B, are shown in red, purple, and blue, respectively.

incomplete removal of the HgTe capping layer from the top surface. The complex physics of the interface between Nb and capped/uncapped HgTe is simplified but, we think, essentially captured by the presence of transverse δ barriers and the absence of longitudinal ones—that is, at the horizontal lines at $s = w + 2h$ and $s = 2(w + h)$ in Fig. 4. Note also that strong barriers throughout would fully suppress Andreev bound states and the associated supercurrent.

Starting from this geometrical model the JJ system is quantum mechanically described by the Bogoliubov–de Gennes Hamiltonian

$$H = \begin{pmatrix} h_e & \Delta e^{i\varphi} \\ \Delta e^{-i\varphi} & h_h \end{pmatrix}, \qquad (2)$$

where h_e and h_h describe the electron and hole Hamiltonians and Δ and φ denote the absolute value and phase of the pairing potential.

The topological surface states are described by the Dirac model Hamiltonian [2,40]

$$h_{e/h} = \pm \hbar v_F \left[\hat{k}_z \sigma_x + \left(\hat{k}_s \pm \frac{\phi}{\phi_0} \frac{\pi}{P} \right) \sigma_y \right] \mp \mu \pm U, \qquad (3)$$

the upper (lower) sign denoting the electron (hole) Hamiltonian. Here, z and s are the coordinates along the wire axis and along the perimeter, and $\hat{k}_z$ and $\hat{k}_s$ the respective momen-

tum operators. Furthermore, μ is the chemical potential and U denotes the barriers at the normal-superconducting (NS) interfaces, see also below.

Only the nanowire surface in direct contact with the superconductor, shaded green in Fig. 4, is affected by the proximity effect. Its bottom surface, grey in Fig. 4, remains normal. Accordingly, the absolute value of the pairing potential is modelled as follows:

$$\Delta = \begin{cases} \Delta_0 & \text{for } 0 \leqslant s \leqslant C \text{ and } -W_S \leqslant z \leqslant 0, \\ \Delta_0 & \text{for } 0 \leqslant s \leqslant C \text{ and } L \leqslant z \leqslant L + W_S, \\ 0 & \text{otherwise.} \end{cases} \qquad (4)$$

Furthermore, we assume that the thickness of the Nb contacts is much smaller than the London penetration depth of Nb such that no supercurrent develops around the perimeter and the magnetic field is not screened. Thus, the superconducting phase φ, defined only in the regions $W_S \leqslant z \leqslant 0$ and $L \leqslant z \leqslant L + W_S$, satisfies

$$\varphi = \begin{cases} -\frac{1}{2}\varphi_0 + 2\pi \frac{\phi}{\phi_0} \frac{s}{P} & \text{for } -W_S \leqslant z \leqslant 0, \\ +\frac{1}{2}\varphi_0 + 2\pi \frac{\phi}{\phi_0} \frac{s}{P} & \text{for } L \leqslant z \leqslant L + W_S \end{cases} \qquad (5)$$

with φ_0 being the phase difference between the superconducting leads across the Josephson junction and the unitary transformation $V(\phi)H(\phi)V^{\dagger}(\phi) = H(0)$ holds for

$$V(\phi) = \exp\left(i\pi \frac{\phi}{\phi_0} \frac{s}{P} \tau_z \right). \qquad (6)$$

The transformation also modifies the boundary condition of the wave function

$$(V\Psi)(s + P) = \pm \exp\left(-i\pi \frac{\phi}{\phi_0} \tau_z \right) (V\Psi)(s), \qquad (7)$$

necessary for the calculation of the Andreev bound states.

Note that Eq. (5) for φ can also be derived using Ginzburg-Landau theory: The free energy density is proportional to the supercurrent $\boldsymbol{J}_S = -2(en_S/m)(\hbar\nabla\varphi + 2e\boldsymbol{A})$. Minimizing $\boldsymbol{J}_S$ leads to $\nabla\varphi = -2e\boldsymbol{A}/\hbar$ [41–43].

B. Semiclassical analysis

1. Method

A semiclassical approach is justified in the limit $k_F L \gg 1$, which is fulfilled in our system, see Sec. IV D. We thus follow the procedure from Ref. [28]. First we identify all classical self-retracing trajectories Γ that arise from pure retro-reflections at the left and right NS contacts. Such trajectories are thus composed of electron-like and hole-like path segments. Each trajectory Γ is then assigned a wave mode bound to a small tube of width $\lambda_F = 2\pi/k_F$ and contributes a current of $j(\Gamma)$ to the total current. The total current follows by integrating the contributions $j(\Gamma)$ over all paths Γ at the Fermi surface. Choosing a cut $z = z_{\text{cut}}$ through the normal part, the paths can be characterized by the s coordinate along this cut and the axial wave number k_s such that the integral reads [28]

$$I = \frac{1}{2\pi} \int ds \int dk_s \, j(s, k_s)$$
$$= \frac{k_F}{2\pi} \int ds \int d\theta \, \cos(\theta) j(s, \theta) \qquad (8)$$

with θ the path angle with respect to the z direction.

The expression (8) contains a significant simplification: It does not account for specular normal reflection at the NS interfaces, which would modify the definition of the current in terms of paths. The inclusion of additional paths from such normal reflections substantially complicates the calculations of $j(\Gamma)$ and I and requires the use of resummation techniques beyond the scope of this work. Moreover, we will establish *a posteriori* via quantum mechanical simulations that only perfectly retro-reflected paths are particularly important. Note also that there is no bending of the paths due to the B-field, since the Lorentz force points perpendicular to the nanowire surface. Finally, for simplicity we stick to the short junction limit, $L \ll \xi = \hbar v_F / \Delta_0$, although we expect our findings to qualitatively hold for long junctions as well.

2. Classification of the trajectories

The classical trajectories can be divided into different categories. First, we can assign a "crossing number" n to each path which counts the crossings through the nonproximitized bottom surface. Formally, one can define a line cut $s = s_{cut}$ with $C < s_{cut} < P$ and count the (directed) crossings through this cut. We emphasize that this integer n does not correspond to a proper winding number around the perimeter. It only counts the transverse crossings of the nonproximitized bottom surface.

Second, we can group the paths according to their start and end points, see Fig. 4:

(1) *Type-1 paths* start and end on the $z = 0$ and $z = L$ NS interfaces;

(2) *Type-2 paths* are "mixed" paths, where start and end points are located on a $z = $ const and a $s = $ const interface;

(3) *Type-3 paths* comprise paths with start and end points on the $s = 0$ and $s = C$ interfaces.

Type-2 paths can be further subdivided into type-2L and type-2R paths, where type-2L paths start on the $z = 0$ interface and type-2R paths end on the $z = L$ interface. It is important to notice that type-2 and type-3 paths only exist for $n \neq 0$, in other words there are only type-1 paths with $n = 0$.

For given initial coordinates (s_0, z_0) and final coordinates (s_1, z_1), the trajectories are parametrized as

$$s(t) = s_0 + t \frac{k_s}{k_F} \quad \text{and} \quad z(t) = z_0 + t \frac{k_z}{k_F}, \quad (9)$$

where the wave numbers satisfy

$$\frac{k_z}{k_s} = \frac{z_1 - z_0}{s_1 - s_0} \quad \text{and} \quad k_z^2 + k_s^2 = k_F^2. \quad (10)$$

3. Current contributions

To calculate the current contribution $j(\Gamma)$ for each classical trajectory Γ, we employ the scattering matrix formalism introduced by Beenakker for one-dimensional Josephson junctions [44]. In the short junction limit $L \to 0$, one gets for the energies of the the Andreev bound states (ABS) [44,45]

$$E = \pm \Delta_0 \sqrt{1 - \tau \sin^2\left(\tfrac{1}{2}\varphi_0 - \gamma\right)}. \quad (11)$$

Here, the gauge-invariant phase difference $\varphi_0 - 2\gamma$ appears [41], where

$$\gamma = \frac{e}{\hbar} \int_\Gamma \mathrm{d}\boldsymbol{s} \cdot \boldsymbol{A} = n\pi \frac{\phi}{\phi_0} \quad (12)$$

is the Aharonov-Bohm (AB) phase of the classical trajectory. In Eq. (12) the parameter τ depends on the transparency and is different for the different types of paths. For zero temperature, the current contribution reads [44,45]

$$j = \frac{e\Delta_0}{4\hbar} \frac{\tau \sin(\varphi_0 - 2\gamma)}{\sqrt{1 - \tau \sin^2(\varphi_0/2 - \gamma)}}, \quad (13)$$

approaching, in the limit $\tau \to 1$,

$$j = \frac{e\Delta_0}{2\hbar} \sin\left(\frac{1}{2}\varphi_0 - \gamma\right) \mathrm{sgn}\left[\cos\left(\frac{1}{2}\varphi_0 - \gamma\right)\right], \quad (14)$$

where sgn is the sign function. For the different types m of paths, one obtains different τ_m, namely,

$$\tau_1 = \frac{1}{\sin^2(\varphi_N) + X^2 \cos^2(\varphi_N)}, \quad (15)$$

$$\tau_2 = \frac{1}{1 + Z^2(1+Z^2)^{-1}\tan^2(\theta)}, \quad \text{and} \quad \tau_3 = 1 \quad (16)$$

with the dimensionless barrier strength $Z = U_0/\hbar v_F$ [34]. The parameters φ_N and X are given by

$$\varphi_N = 2\arctan\left(\frac{\cos(\theta) + Z\tan(\theta)}{Z - \sin(\theta) - [1 + Z^2 + Z^2\tan^2(\theta)]^{1/2}}\right) \quad (17)$$

and

$$X = [1 + 2Z^2(1+Z^2)^{-1}\tan^2(\theta)]. \quad (18)$$

C. Numerical simulations

Besides the semiclassical approach we also employ numerical tight-binding simulations with the PYTHON package Kwant [46]. Using the finite difference method, the BdG Hamiltonian Eq. (2) and its components, consisting of nontrivial surface states with a linear dispersion Eq. (3), are evaluated on a discrete square grid with lattice constant a. Note that by putting the Dirac Hamiltonian on a lattice, the well-known Fermion doubling problem arises [47–51]. This issue can be circumvented by considering an additional Wilson mass term $H_W = E_W a/(4\hbar v_F)(k_z^2 + k_s^2)\sigma_z$ [47,52], which gaps out the artificial Dirac cones at the borders of the first Brillouin zone. This term is important to avoid nonphysical intervalley scattering introduced by the potential barriers $U(z, s)$, Eq. (1), in the JJ. Also, regarding these δ barriers, one has to appropriately scale the amplitude for the discrete representation. This is achieved by fixing $U_0' = U_0/a$.

Connecting the lattice sites with coordinates $(z, s = 0)$ and $(z, s = P)$ by a hopping with phase factor $\exp(i\pi)$ we introduce antiperiodic boundary conditions. Moreover, the flux through the wire cross section is accounted for by a Peierls substitution with the additional phase factor $\exp(i2\pi \frac{a}{P} \frac{\phi}{2\phi_0})$.

Finally, superconductivity is introduced as simple on site s-wave pairing given by Eq. (4). For the numerics we assume semi-infinite leads, i.e., $W_s \to \infty$, because we directly attach translationally invariant superconducting leads to the normal
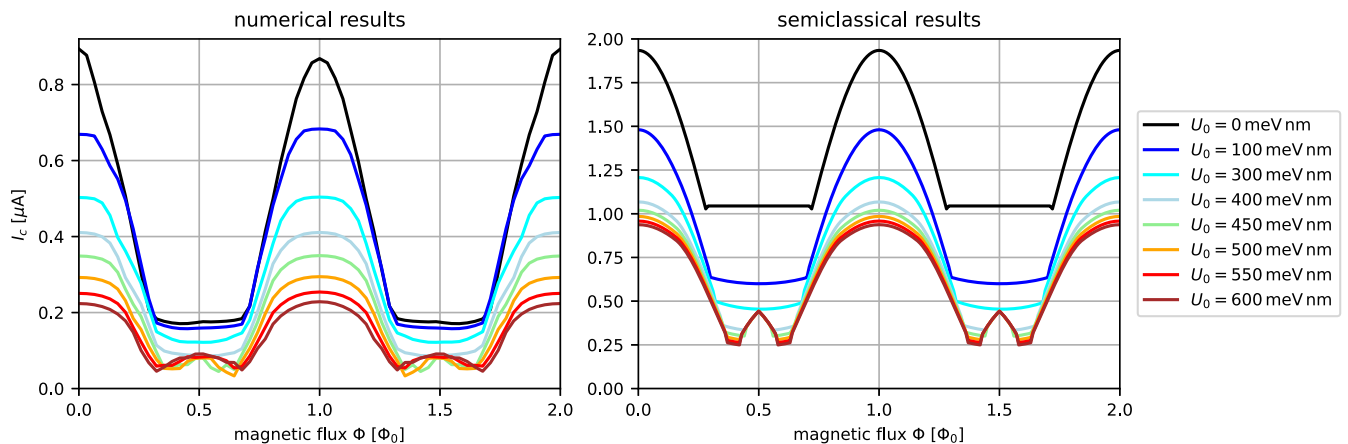
FIG. 5. Critical current for the TI nanowire-based Josephson junction. The results from the semiclassical (left panel) and numerical calculations (right) are shown for four different strengths of the interfacial barrier potential, Eq. (1). The barrier predominantly suppresses contributions from direct paths which do not cross the bottom surface of the wire, such that the peaks at $\phi = h/4e = \phi_0/2$ and $3h/4e = 3\phi_0/2$ emerge. For larger barrier strengths, those peaks start to appear and become observable in comparison to the peaks at integer multiples of ϕ_0.

JJ part to keep the numerical cost to a minimum. Additionally, we consider the local phase modulation of Δ introduced in Eq. (5).

To access the current-phase relation and incorporate all geometrical junction details we compute the supercurrent following Ref. [53]. Furthermore we exploit part of the code package provided in a repository of Ref. [19], and adapt it to our implemented tight-binding model. The core of the numerical method is the computation of the current-phase relation via Green's functions. The supercurrent is given by

$$I_{LR}(\varphi_0, \phi) = 2 \frac{e k_B T}{\hbar} \sum_{n=0}^{\infty} \sum_{\substack{i \in R \\ j \in L}} \text{Im}\big(H_{ji} G_{ij}^r(i\omega_n) - H_{ij} G_{ji}^r(i\omega_n)\big),$$

(19)

where $\omega_n = \frac{k_B T}{\hbar}(2n+1)\pi$ are fermionic Matsubara frequencies. The labels i and j run over lattice sites in two adjacent transversal lattice rows R and L. In Eq. (19) the terms H_{ij} and G_{ij} denote the hopping matrix elements and the off-diagonal elements of Green's function, respectively, connecting those sites. Furthermore, the phase difference φ_0 is incorporated into the hopping matrix elements as a phase factor. This is simply introduced by performing a gauge transformation that shifts the phase difference into a vector potential inside the JJ. For more details of the methodology we refer the reader to Refs. [19,28]. For a fixed magnetic flux, the critical current is

$$I_c(\phi) = \max_{\varphi_0} |I_{LR}(\varphi_0, \phi)|,$$

(20)

i.e., the maximum of the corresponding current-phase relation.

D. Semiclassical and numerical results for the critical current

We are now in a position to combine semiclassics and quantum mechanical simulations to explain the central experimental findings for the critical current reported in Sec. III. For the realistic JJ setup discussed in Sec. IV A we choose the following parameters to model the SNS-junction geometry, see Fig. 4: $w = 300$ nm, $h = 80$ nm, $L = 100$ nm, $W_S = 1000$ nm, $\hbar v_F = 330$ meV nm, $\mu = 30$ meV, and $\Delta_0 = 0.8$ meV, in

accordance with Refs. [17,31,54]. The corresponding Fermi wave number is $k_F \approx 0.09$ nm^{-1}, i.e., the Fermi wavelength $\lambda_F \sim 70$ nm, and $k_F L \approx 10$. Hence, the semiclassical limit ($k_F L \gg 1$) is well justified. Since the coherence length reads $\xi \approx 400$ nm, working in the short junction limit is also justified. In the semiclassical calculations we include only paths with crossing numbers $n = 0, \pm 1$, since their angle θ is small and maximizes the $\cos\theta$ factor in the integral (8). Paths with higher crossing number $|n|$ have lower weight, and indeed we checked that including them modifies our results only marginally. Furthermore higher-crossing paths quickly approach the coherence length cutoff, i.e., phase coherence is lost before the electron crosses the junction. The value of μ is chosen to have a high number of open channels while still keeping the numerical simulations in an energetically converged regime.

Numerical and semiclassical results for the critical current are shown and compared to each other in Fig. 5. On the whole the numerics (left panel) and semiclassics (right panel) show qualitative agreement. It is convenient to start by looking at the numerics, which show peaks only at integer values of $\phi_0 = h/2e$ in the case of perfect interface transparency, i.e., without any barrier ($U_0 = 0$). We note that in high transparency samples no oscillation was measured at all. Our theory model predicts no oscillation for fully proximitized systems, which is indeed more likely when the NS junction is good. In a fully proximitized nanowire there is no phase variation around the perimeter, except in integer multiples of 2π, describing a vortex. Without any kind of accounting for the vector potential in the superconducting phase, the gap and therefore also the critical current will show just an exponential decay. Fully capturing the dependence of the spatial extend of the proximity induced gap in the TI nanowire requires a detailed modeling of the complex hybrid structure. This problem deserves attention on its own and does not belong here. Our effective model includes the proximity effect on a phenomenological footing and can capture the relevant physical signatures, i.e., monotonous decay or periodic oscillations of the supercurrent, by adjusting the relevant parameters. This is also directly

related to the assumption of simple δ-like barriers, which suppress the junction transparency.

Moreover, we note that panels c, d, and e of Fig. 3 show shoulder like features, which correspond to an intermediate regime between the monotonous decay and the regime of clear-cut oscillations. Our model can also be adjusted to show such supercurrent features. However, it is necessary to assume an additional parameter describing a local gating in the proximitized regions. This corresponds to a local band bending due to the different Fermi energies in niobium and HgTe. This aspect is not treated in this work, as we concentrate on the oscillatory component and do not address this specific signature. In summary, our model is not microscopically sample-tailored for a precise quantitative analysis, but gives general insight into the necessary physical properties of JJs behind the observed flux-periodic supercurrent oscillations.

For increasing barrier strength U_0, the interfacial transparencies $\tau_{1,2}$ decrease, leading to an overall reduction of the critical current. At the same time, with increasing U_0 new maxima emerge and grow at fluxes $\phi = h/4e = \phi_0/2$ and $3h/4e = 3\phi_0/2$, reaching a peak height of nearly one-half the major peaks (for $U_0 = 600$ meVnm).

The semiclassical results from the right panel of Fig. 5 show a corresponding trend: a decreasing critical current with increasing barrier height and the emergence of additional peaks at $\phi = h/4e$ and $3h/4e$. In the semiclassical calculation the dominant peaks arise mainly from the short lead-connecting trajectories marked as type-1 paths with crossing number $n = 1$ in Fig. 4. Upon increasing the barrier height contributions from such type-1 paths are suppressed relative to those from type-2 and type-3 paths with $n = \pm 1$, since the former involve two barrier reflections while the latter only one, or none at all. For instance, the current associated with type-3 paths is not influenced by the barrier at all. The growing relevance of paths with $n = \pm 1$ and no barrier reflection leads to the emergence of the peaks at $h/4e$ and to their increase relative to the peaks at $h/2e$.

To conclude the comparison, semiclassical and numerical results agree on the fundamental aspects: they both predict the emergence of peculiar $h/4e$ peaks for larger barrier strength U_0, the increase of their magnitude relative to the $h/2e$ peaks, and the broadening of all peaks with increasing U_0.

A few differences between them, however, remain: Numerics give a considerably smaller value of the current, and the peak current also decreases faster with increasing barrier strength U_0. With regard to this, first note that the actually induced "effective" gap of each of the ABSs as obtained in the numerical calculations is smaller than Δ_0; see the Appendix for a detailed discussion. To fix this issue in the semiclassical calculation, one would need to introduce an effective gap $\Delta_{eff} < \Delta_0$ (possibly different for each mode). Second, as mentioned in Sec. IV B 1 the semiclassical method neglects contributions from paths with normal specular reflection. We expect the resulting effects to reduce the current further, as more normal electron reflection reduces the contribution of Andreev reflection. Furthermore, numerics is not limited to the short junction limit, and in fact fully captures effects of finite length and finite temperature. For shorter junctions the difference between the semiclassical and numerical current magnitude is indeed smaller, an explicit hint that the short

junction assumption of semiclassics loses accuracy for longer systems.

To conclude the theory discussion, the semiclassical approach is approximate but enables us to interpret the different peculiar peaks in terms of specific (quantized) relevant families of trajectories. The emergence of the additional peaks related to paths (partially) winding around the nanowire highlights the three-dimensional character of the SNS junction geometry, compared to common planar junctions.

V. COMPARISON OF EXPERIMENT AND THEORY

We finally compare the experimentally measured critical currents with the corresponding theoretically calculated results.

Consider first measurements for samples with high average transparency, as shown in Fig. 3(a), 3(b). The experimental results exhibit a monotonous decay of the critical current, while our theoretical results for high transparency, corresponding to $U_0 = 0$, show clear oscillations with period $h/2e$, see the uppermost black curve in Fig. 5(a). This apparent discrepancy between experiment and theory can be related to the fact that the measurements on high-transparency samples are not appropriately described by our model geometry (Fig. 4), where superconductivity is not induced around the whole circumference. However, as mentioned in Sec. IV A, a high-quality NS interface allows for superconducting pairing to be induced along the entire nanowire perimeter. Indeed, if we adapt our model geometry and assume a closed external superconducting shell, i.e., superconducting pairing developed around the full circumference, we find numerically (not shown) that the critical current decays exponentially without any oscillation, as observed in the high-transparency samples. In such a model geometry, there can be no phase variation around the perimeter, as given by Eq. (5), and the Andreev bound states become similar to those of planar Josephson junctions. In such a scenario the magnetic field simply destroys the pair correlations, and the superconducting gap decreases monotonically with increasing field strength leading to the corresponding decrease of the critical current.

On the contrary, flux periodic supercurrent oscillations are observed in samples with low average transparency. In Sec. IV A we argued that the junction transparency might be reduced due to an imperfect removal of a capping layer, which lowers the interface quality between the superconducting Nb and HgTe. The imperfect interface was modelled both semiclassically and numerically via barriers of varying strength, whose presence suppresses the large current contributions which have no or only a $h/2e$ periodicity. Vice versa, the $h/4e$-periodic current components are not affected and their signatures emerge, providing a clear explanation for the observed behavior of low-transparency junctions.

Irrespective of the sample quality, all measurements show also a decrease of the current for increasing magnetic field. This is expected and attributed to the reduction of the induced superconducting gap by the magnetic field [13], which weakens pairing correlations. One can phenomenologically account for this behavior by multiplying the theoretical data with an appropriate envelope function, mimicking the
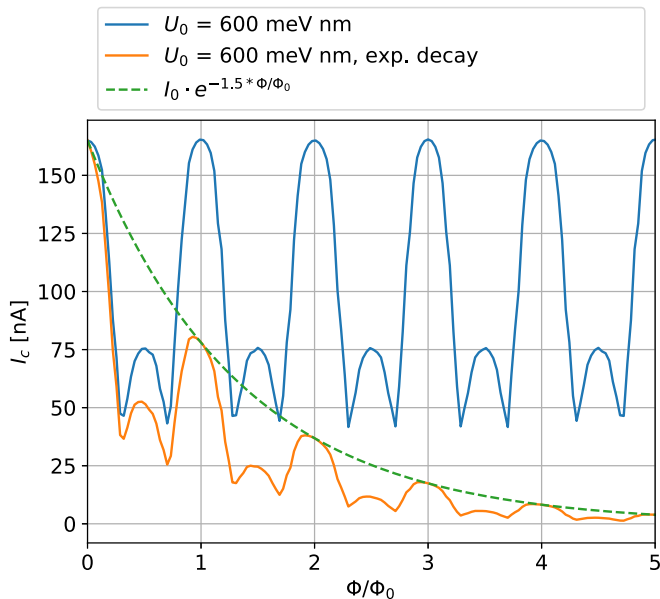
FIG. 6. Introducing an exponential envelope function to mimic the pair breaking mechanism of the applied flux leads to a good agreement between theoretical results and the experimental observations. The blue curve corresponds to the originally calculated numerical data, while the orange curve shows the adjusted data.

weakening of the BdG pairing amplitude Δ_0 of Eq. (4).[3] An example is shown in Fig. 6, where we assumed a simple exponential decay of the pairing potential with respect to the applied flux. The data were numerically computed with the same system parameters as for Fig. 5, except that the length was increased to $L = 200$ nm to better match the experimental dimensions. The blue curve is the raw simulation data, while the orange one is adjusted with the phenomenological flux-induced decay. The adjusted critical current exhibits all qualitative features of the experimental curve plotted in Fig. 3(g). In particular the peak at $\phi/\phi_0 = 1$ is larger than the first half-integer one.

We further remark that also oscillations with a period of $h/8e$ were observed in sample G. From the semiclassical model such a periodicity is to be expected if paths with crossing number $n = \pm 2$ contribute considerably to the current flow. This should be possible in the presence of a large overall number of conducting channels, with sufficiently many belonging to the $n = \pm 2$ family to make their signature visible—recall that such paths are identified by a large angle θ, such that the weight of a single path in Eq. (8) is usually very low. This agrees with the observation that sample G has indeed the highest number of open transport channels. Our argument is also in line with the behavior from sample J: A gating potential of $V_G = 3$ V has to be applied to the junction, such that the $h/4e$ periodic oscillations can be measured. The gating potential increases the Fermi energy, ergo the number of open transport channels. As a consequence the

contribution of type-2 and type-3 paths grows and maxima at $\phi = (2n + 1) \cdot \phi_0/2$ appear.

VI. CONCLUSIONS

We realized Josephson junctions made of HgTe 3D topological insulator nanowires and demonstrated the fine sensitivity of surface supercurrents to a coaxial magnetic field. The field does not pierce the topologically protected surface states of the wires, yet Fraunhofer-like critical current patterns develop, notably with unusual noninteger flux periodicity in lower-quality samples. Our theoretical analysis shows that such peculiar magnetotransport properties are essentially resulting from a series of nontrivial geometrical constraints. First, contrary to standard Josephson junctions, propagating electronic modes form Andreev bound states uniquely on a nonplanar surface enclosing the insulating HgTe bulk. Second, such states may have a purely longitudinal character—associated with semiclassical paths roughly parallel to the axial direction—or a partially transverse behavior—corresponding to paths winding fully or partially around the wire perimeter—and are differently affected by the quality of the NS contacts along different directions. Third, superconductivity is in general not induced across the entire nanowire perimeter, nor is the magnetic field screened by the Nb fingers, which are thinner than the London penetration depth. As a consequence the partially transverse Andreev bound states pick up an Aharonov-Bohm phase which is not necessarily integer, i.e., electrons are not limited to enclosing a fixed number of vortices. This yields the observed peculiar critical current oscillations.

On the other hand, while the existence of surface states is necessary, spin-momentum locking of topological Dirac states appears to play a minor role. We numerically found similar overall features for surface states obeying an effective Schrödinger equation.

For further studies it is certainly desirable and interesting also to measure the current-phase relation. Due to the Aharonov-Bohm phase, which is picked up by the Andreev bound states, related signatures could be observable in such measurements and serve as an additional check for the theoretical model.

APPENDIX: NUMERICAL CALCULATION OF ANDREEV BOUND STATE SPECTRA FOR PARTIALLY COVERED NANOWIRES

The difference in current magnitude of the semiclassical analytical approach and the numerical data can be partially

---

[3]A microscopic description would require a self-consistent treatment of the superconductor in its electromagnetic environment, which is beyond the scope of the present work.

explained by the difference in the spectra of the ABS. For the analytical approach the ABS spectrum for each mode is assumed to be given by the standard expression Eq. (11), where the amplitude factor is determined by a constant gap Δ_0. However, in the numerical calculation, this is not the case. Due to the partial coverage of the nanowire circumference with the s-wave superconductor, each mode in the surface state spectrum experiences an effective induced gap. We can show this by numerically computing the ABS spectrum of such a system. The eigenenergies of this nanowire Josephson junction can be determined by diagonalization of a finite tight-binding system with long superconducting reservoirs. The advantage of this method is the natural incorporation of the complex geometry. The superconducting reservoirs are connected by a periodic boundary hopping, where the superconducting phase difference enters again in a longitudinal hopping in the center of the normal region. In Figs. 7(a) and 7(b) the calculated ABS spectra are plotted for $U_0 = 0$ and $U_0 = 600\,\mathrm{meVnm}$, respectively. For simplicity we neglect here the axial magnetic flux and choose a relatively narrow nanowire with width $w = 120\,\mathrm{nm}$. The reason for that lies in the reduced number of open sub-bands, such that the relevant spectrum features are more clearly observable. Again we assume that the top, as well as the side surfaces are proximitized by the external s-wave superconductor, while the wire bottom remains normal conducting. Note that the ABS energies are normalized by Δ_0. In Fig. 7(a) we see that the ABS spectrum remains ungapped due to the missing barriers. Still, contrary to standard clean Josephson junctions, the ABS branches for different modes are no longer degenerate. At phase difference zero, where the energies are typically located at the band gap Δ_0, the different branches exhibit very different values. This indicates that each mode experiences a different effective pairing strength, depending on their angular momentum quantum number. Also, the values at $\varphi_0 = 0$ differ quite strongly from Δ_0, which is used in the semiclassical analysis. Therefore, the difference in current magnitude between numerics and semiclassics can be partially explained by the simplified assumption of a constant superconducting gap in the ABS energies in the latter case. This holds also true for the case of a non-zero barrier, which is illustrated in Fig. 7(b). The differently induced gaps for each mode are still present, only the spectra become gapped at a phase difference of $\varphi_0 = \pi$.
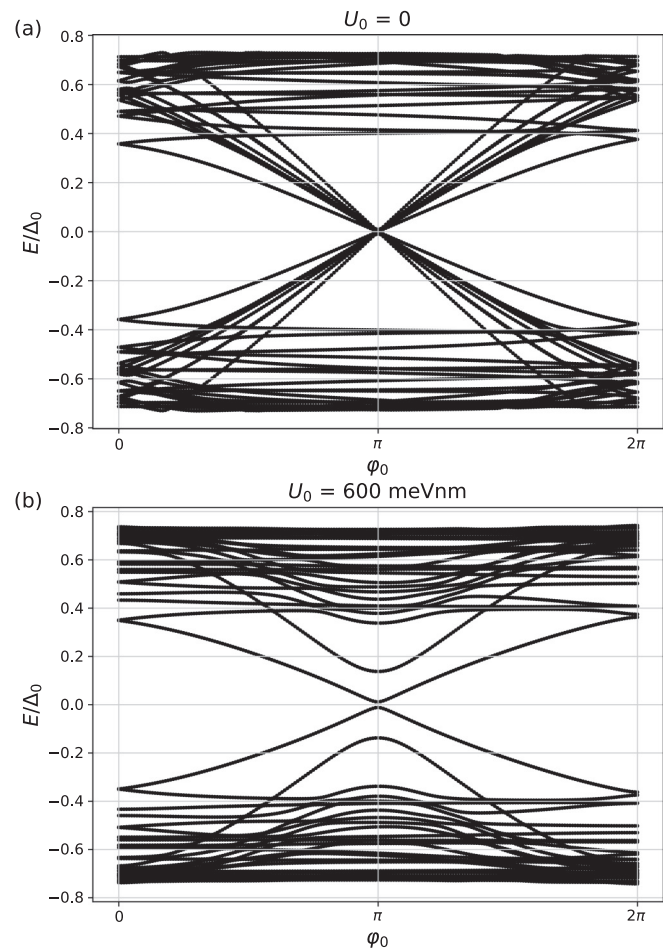

FIG. 7. Andreev bound state spectrum of a TI Josephson junction which is partially covered by an s-wave superconductor (see Fig. 4). The wire has a width $w = 120\,\mathrm{nm}$ and a height $h = 80\,\mathrm{nm}$, while the junctions have a length of $L = 200\,\mathrm{nm}$. The lattice constant is fixed to $a = 5\,\mathrm{nm}$ and the chemical potential is set to $\mu = 22\,\mathrm{meV}$. In (a) the local barrier strength is set to zero, while in (b) the barrier value is set to $U_0 = 600\,\mathrm{meVnm}$. For both panels the axial magnetic field is set to zero. The spectrum is computed by diagonalization of a finite tight-binding system. Due to the partial covering the branches in the spectrum have different effective gaps Δ_{eff}. This explains the difference in the current of the numerical and analytical calculations.

[1] P. M. Ostrovsky, I. V. Gornyi, and A. D. Mirlin, Interaction-induced criticality in $\mathbb{Z}_2$ topological insulators, Phys. Rev. Lett. **105**, 036803 (2010).

[2] J. H. Bardarson, P. W. Brouwer, and J. E. Moore, Aharonov-bohm oscillations in disordered topological insulator nanowires, Phys. Rev. Lett. **105**, 156803 (2010).

[3] J. H. Bardarson and J. E. Moore, Quantum interference and Aharonov–Bohm oscillations in topological insulators, Rep. Prog. Phys. **76**, 056501 (2013).

[4] R. Kozlovsky, A. Graf, D. Kochan, K. Richter, and C. Gorini, Magnetoconductance, quantum Hall effect, and coulomb blockade in topological insulator nanocones, Phys. Rev. Lett. **124**, 126804 (2020).

[5] A. Graf, R. Kozlovsky, K. Richter, and C. Gorini, Theory of magnetotransport in shaped topological insulator nanowires, Phys. Rev. B **102**, 165105 (2020).

[6] V. Mourik, K. Zuo, S. M. Frolov, S. R. Plissard, E. P. A. M. Bakkers, and L. P. Kouwenhoven, Signatures of Majorana fermions in hybrid superconductor-semiconductor nanowire devices, Science **336**, 1003 (2012).

[7] L. P. Rokhinson, X. Liu, and J. K. Furdyna, The fractional a.c. Josephson effect in a semiconductor–superconductor nanowire as a signature of Majorana particles, Nat. Phys. **8**, 795 (2012).

[8] M. T. Deng, S. Vaitiekėnas, E. B. Hansen, J. Danon, M. Leijnse, K. Flensberg, J. Nygård, P. Krogstrup, and C. M. Marcus, Majorana bound state in a coupled quantum-dot hybrid-nanowire system, Science **354**, 1557 (2016).

[9] Ö. Gül, H. Zhang, J. D. S. Bommer, M. W. A. de Moor, D. Car, S. R. Plissard, E. P. A. M. Bakkers, A. Geresdi, K. Watanabe, T. Taniguchi, and L. P. Kouwenhoven, Ballistic Majorana nanowire devices, Nat. Nanotechnol. **13**, 192 (2018).

[10] A. M. Cook, M. M. Vazifeh, and M. Franz, Stability of Majorana fermions in proximity-coupled topological insulator nanowires, Phys. Rev. B **86**, 155431 (2012).

[11] R. Ilan, J. H. Bardarson, H.-S. Sim, and J. E. Moore, Detecting perfect transmission in Josephson junctions on the surface of three dimensional topological insulators, New J. Phys. **16**, 053007 (2014).

[12] F. de Juan, R. Ilan, and J. H. Bardarson, Robust transport signatures of topological superconductivity in topological insulator nanowires, Phys. Rev. Lett. **113**, 107003 (2014).

[13] F. de Juan, J. H. Bardarson, and R. Ilan, Conditions for fully gapped topological superconductivity in topological insulator nanowires, SciPost Phys. **6**, 060 (2019).

[14] E. Xypakis, J.-W. Rhim, J. H. Bardarson, and R. Ilan, Perfect transmission and Aharanov-Bohm oscillations in topological insulator nanowires with nonuniform cross section, Phys. Rev. B **101**, 045401 (2020).

[15] H. F. Legg, D. Loss, and J. Klinovaja, Majorana bound states in topological insulators without a vortex, Phys. Rev. B **104**, 165405 (2021).

[16] H. F. Legg, D. Loss, and J. Klinovaja, Metallization and proximity superconductivity in topological insulator nanowires, Phys. Rev. B **105**, 155413 (2022).

[17] R. Fischer, J. Picó-Cortés, W. Himmler, G. Platero, M. Grifoni, D. A. Kozlov, N. N. Mikhailov, S. A. Dvoretsky, C. Strunk, and D. Weiss, 4π-periodic supercurrent tuned by an axial magnetic flux in topological insulator nanowires, Phys. Rev. Res. **4**, 013087 (2022).

[18] H. J. Suominen, J. Danon, M. Kjaergaard, K. Flensberg, J. Shabani, C. J. Palmstrøm, F. Nichele, and C. M. Marcus, Anomalous Fraunhofer interference in epitaxial superconductor-semiconductor Josephson junctions, Phys. Rev. B **95**, 035307 (2017).

[19] K. Zuo, V. Mourik, D. B. Szombati, B. Nijholt, D. J. van Woerkom, A. Geresdi, J. Chen, V. P. Ostroukh, A. R. Akhmerov, S. R. Plissard, D. Car, E. P. A. M. Bakkers, D. I. Pikulin, L. P. Kouwenhoven, and S. M. Frolov, Supercurrent interference in few-mode nanowire Josephson junctions, Phys. Rev. Lett. **119**, 187704 (2017).

[20] K. Gharavi, G. W. Holloway, R. R. LaPierre, and J. Baugh, Nb/InAs nanowire proximity junctions from Josephson to quantum dot regimes, Nanotechnology **28**, 085202 (2017).

[21] P. Sriram, S. S. Kalantre, K. Gharavi, J. Baugh, and B. Muralidharan, Supercurrent interference in semiconductor nanowire Josephson junctions, Phys. Rev. B **100**, 155431 (2019).

[22] A. Kringhøj, G. W. Winkler, T. W. Larsen, D. Sabonis, O. Erlandsson, P. Krogstrup, B. van Heck, K. D. Petersson, and C. M. Marcus, Andreev modes from phase winding in a full-shell nanowire-based transmon, Phys. Rev. Lett. **126**, 047701 (2021).

[23] P. Perla, H. A. Fonseka, P. Zellekens, R. Deacon, Y. Han, J. Kölzer, T. Mörstedt, B. Bennemann, A. Espiari, K. Ishibashi, D. Grützmacher, A. M. Sanchez, M. I. Lepsa, and T. Schäpers, Fully in situ Nb/InAs-nanowire Josephson junctions

by selective-area growth and shadow evaporation, Nanoscale Adv. **3**, 1413 (2021).

[24] L. Stampfer, D. J. Carrad, D. Olsteins, C. E. N. Petersen, S. A. Khan, P. Krogstrup, and T. S. Jespersen, Andreev interference in the surface accumulation layer of half-shell InAsSb/Al hybrid nanowires, Adv. Mater. **34**, 2108878 (2022).

[25] C.-Z. Li, A.-Q. Wang, C. Li, W.-Z. Zheng, A. Brinkman, D.-P. Yu, and Z.-M. Liao, Topological transition of superconductivity in Dirac semimetal nanowire Josephson junctions, Phys. Rev. Lett. **126**, 027001 (2021).

[26] A. Q. Chen, M. J. Park, S. T. Gill, Y. Xiao, D. Reig-i-Plessis, G. J. MacDougall, M. J. Gilbert, and N. Mason, Finite momentum Cooper pairing in three-dimensional topological insulator Josephson junctions, Nat. Commun. **9**, 3478 (2018).

[27] P. Schüffelgen, D. Rosenbach, C. Li, T. W. Schmitt, M. Schleenvoigt, A. R. Jalil, S. Schmitt, J. Kölzer, M. Wang, B. Bennemann, U. Parlak, L. Kibkalo, S. Trellenkamp, T. Grap, D. Meertens, M. Luysberg, G. Mussler, E. Berenschot, N. Tas, A. A. Golubov *et al.*, Selective area growth and stencil lithography for *in situ* fabricated quantum devices, Nat. Nanotechnol. **14**, 825 (2019).

[28] V. P. Ostroukh, B. Baxevanis, A. R. Akhmerov, and C. W. J. Beenakker, Two-dimensional Josephson vortex lattice and anomalously slow decay of the Fraunhofer oscillations in a ballistic SNS junction with a warped Fermi surface, Phys. Rev. B **94**, 094514 (2016).

[29] H. Courtois, P. Gandit, D. Mailly, and B. Pannetier, Long-range coherence in a mesoscopic metal near a superconducting interface, Phys. Rev. Lett. **76**, 130 (1996).

[30] D. A. Kozlov, Z. D. Kvon, E. B. Olshanetsky, N. N. Mikhailov, S. A. Dvoretsky, and D. Weiss, Transport properties of a 3D topological insulator based on a strained high-mobility HgTe film, Phys. Rev. Lett. **112**, 196801 (2014).

[31] J. Ziegler, R. Kozlovsky, C. Gorini, M.-H. Liu, S. Weishäupl, H. Maier, R. Fischer, D. A. Kozlov, Z. D. Kvon, N. Mikhailov, S. A. Dvoretsky, K. Richter, and D. Weiss, Probing spin helical surface states in topological HgTe nanowires, Phys. Rev. B **97**, 035157 (2018).

[32] C. P. Scheller, S. Heizmann, K. Bedner, D. Giss, M. Meschke, D. M. Zumbühl, J. D. Zimmerman, and A. C. Gossard, Silver-epoxy microwave filters and thermalizers for millikelvin experiments, Appl. Phys. Lett. **104**, 211106 (2014).

[33] G. E. Blonder, M. Tinkham, and T. M. Klapwijk, Transition from metallic to tunneling regimes in superconducting microconstrictions: Excess current, charge imbalance, and supercurrent conversion, Phys. Rev. B **25**, 4515 (1982).

[34] M. Octavio, M. Tinkham, G. E. Blonder, and T. M. Klapwijk, Subharmonic energy-gap structure in superconducting constrictions, Phys. Rev. B **27**, 6739 (1983).

[35] G. Niebler, G. Cuniberti, and T. Novotný, Analytical calculation of the excess current in the Octavio-Tinkham-Blonder-Klapwijk theory, Supercond. Sci. Technol. **22**, 085016 (2009).

[36] K. Flensberg, J. B. Hansen, and M. Octavio, Subharmonic energy-gap structure in superconducting weak links, Phys. Rev. B **38**, 8707 (1988).

[37] S.-K. Yip, Magnetic-field effect on the supercurrent of an SNS junction, Phys. Rev. B **62**, R6127 (2000).

[38] T. T. Heikkilä, F. K. Wilhelm, and G. Schön, Non-equilibrium supercurrent through mesoscopic ferromagnetic weak links, Europhys. Lett. **51**, 434 (2000).

[39] M. S. Crosser, J. Huang, F. Pierre, P. Virtanen, T. T. Heikkilä, F. K. Wilhelm, and N. O. Birge, Nonequilibrium transport in mesoscopic multi-terminal SNS Josephson junctions, Phys. Rev. B **77**, 014528 (2008).

[40] Y. Zhang and A. Vishwanath, Anomalous Aharonov-Bohm conductance oscillations from topological insulator surface states, Phys. Rev. Lett. **105**, 206601 (2010).

[41] M. Tinkham, *Introduction to Superconductivity*, 2nd ed. (McGraw-Hill, New York, 1996).

[42] P. Wójcik and M. P. Nowak, Durability of the superconducting gap in Majorana nanowires under orbital effects of a magnetic field, Phys. Rev. B **97**, 235445 (2018).

[43] G. W. Winkler, A. E. Antipov, B. van Heck, A. A. Soluyanov, L. I. Glazman, M. Wimmer, and R. M. Lutchyn, Unified numerical approach to topological semiconductor-superconductor heterostructures, Phys. Rev. B **99**, 245408 (2019).

[44] C. W. J. Beenakker, Universal limit of critical-current fluctuations in mesoscopic Josephson junctions, Phys. Rev. Lett. **67**, 3836 (1991).

[45] T. M. Klapwijk, Proximity effect from an Andreev perspective, J. Supercond. **17**, 593 (2004).

[46] C. W. Groth, M. Wimmer, A. R. Akhmerov, and X. Waintal, Kwant: A software package for quantum transport, New J. Phys. **16**, 063065 (2014).

[47] L. Susskind, Lattice fermions, Phys. Rev. D **16**, 3031 (1977).

[48] R. Stacey, Eliminating lattice fermion doubling, Phys. Rev. D **26**, 468 (1982).

[49] H. Nielsen and M. Ninomiya, A no-go theorem for regularizing chiral fermions, Phys. Lett. B **105**, 219 (1981).

[50] H. Nielsen and M. Ninomiya, Absence of neutrinos on a lattice: (I). Proof by homotopy theory, Nucl. Phys. B **185**, 20 (1981).

[51] H. Nielsen and M. Ninomiya, Absence of neutrinos on a lattice: (II). Intuitive topological proof, Nucl. Phys. B **193**, 173 (1981).

[52] K. M. M. Habib, R. N. Sajjad, and A. W. Ghosh, Modified Dirac Hamiltonian for efficient quantum mechanical simulations of micron sized devices, Appl. Phys. Lett. **108**, 113105 (2016).

[53] A. Furusaki, DC Josephson effect in dirty SNS junctions: Numerical study, Phys. B: Condens. Matter **203**, 214 (1994).

[54] J. Fuchs, M. Barth, C. Gorini, I. Adagideli, and K. Richter, Crossed Andreev reflection in topological insulator nanowire T junctions, Phys. Rev. B **104**, 085415 (2021).